A Novel Micromechanical Rock-pile Interface Model with Application to Rock-socketed Pile Modeling

Rui LIANG, Zhen-Yu YIN and Jian-Hua YIN

Department of Civil and Environmental Engineering, The Hong Kong Polytechnic University, Hong Kong, China.

doi: https://doi.org/10.21467/proceedings.7.7.7

ABSTRACT

The increasing use of rock-socketed piles highlights the importance of developing a suitable design method for their bearing capacity. This study quantifies the shear behavior of the rock-pile interface, which generally dominates the bearing capacity of rock-socketed piles under service load. A micromechanics-based rock-pile interface model with idealized nonuniform profile is proposed with two enhancements: (1) the slip line method together with nonlinear Hoek-Brown failure criteria is integrated to identify the critical shear displacement of rock asperity; and (2) the residual stage of shear behavior is properly considered with the rounding progress of sheared rubbles. Then, the interface model is implemented via user defined FRIC into the finite element code ABAQUS without the need of explicitly building the rock-pile interface profile. Comparison between the predictions and field observed results shows this method can well capture the axial load transfer behavior of pile socket into weak rock. Comparison between the predictions and field observed results shows this method can well capture the axial load transfer behavior of pile socket into weak rock.

1 INTRODUCTION

Rock-socketed bored piles are widely used to support superstructures due to the high axial capacity from both side and toe resistance from the portion of the pile embedded into rock socket (BD (Buildings Department Technical Committee of Hong Kong) 2017). The shaft resistance of drilled rock sockets typically bear a major proportion of working load on the piles, which can account for 80-85% of their total capacity (Chen et al. 2021). This is due to the fact that the mobilized displacement between the shaft and surrounding rock required for the ultimate shaft resistance is smaller than that for the ultimate toe resistance (Carter and Kulhawy 1988). Therefore, predicting pile shaft shear behavior is more critical than predicting toe resistance (Seol et al. 2009, Akgüner and Kirkit 2012). Numerous experimental studies have been conducted to investigate the performance of side resistance on drilled shafts embedded in rocks (Williams 1980, Leung and Ko 1993, O'Neill et al. 1996, Dykeman and Valsangkar 1996, Carrubba 1997, Zhan and Yin 2000, Ng et al. 2001, Omer et al. 2002, Kou et al. 2016, Dai et al. 2017, Xu et al. 2020, Chen et al. 2021). The investigation of influence factors such as test pile details (e.g., pile dimension, socket depth and construction techniques), rock mass characteristics (e.g., rock types and rock stiffness) and rock-pile interface roughness have been reported. However, the lack of detailed information about the constructed socket profile in most of these studies makes it difficult to quantitatively analyze the impact of socket-pile interface roughness on pile side resistance, despite interface roughness being the primary factor influencing shaft friction.

Several interface models (Castelli et al. 1992, O'Neill and Hassan 1994, Seidel and Haberfield 2002, Seol et al. 2009, Tian et al. 2015, Li et al. 2019, Zhao et al. 2022) have been proposed to predict the shear mechanisms between pile shaft and rock joints based on numerous studies and shear tests conducted under constant normal stress (CNS) and constant normal stiffness (CNS) boundary conditions. O'Neill and Hassan

Proceedings DOI: 10.21467/proceedings.7.7; Series: AIJR Proceedings; ISSN: 2582-3922; ISBN: 978-81-989164-3-3

(1994) suggested a hyperbolic shear functions that considers the pile diameter and Young's modulus of the rock. Seol et al. (2009) employed a nonlinear triple-curve model to describe the shear load-transfer characteristics of the rock-socketed pile shaft based on the Hoek-Brown failure criterion. Tian et al. (2015) presented an interface model that considers the elastic stage of cohesive bond and the post-peak stage due to the bond failure and increasing friction. Li et al. (2019) proposed an analytical model for rock joint shear behavior consisting of waviness and unevenness asperities separated by wavelet analysis.

The shear mechanism of the rock-socketed pile shaft is of particular interest in this study. The motivation of this paper is to develop a rock-pile interface model and provide a valuable method to calculate the axial bearing capacity of piles socketed into weak rock, since the weathered rock layer is widespread in Hong Kong (Ng et al. 2001). In this paper, a micromechanically based interface model focusing on the shear behavior between the pile shaft and weak rock has been proposed considering rock mass with nonlinear failure criteria with two enhancements: (1) the slip line method together with nonlinear Hoek-Brown failure criteria has been integrated to identify the critical shear displacement of rock asperity; and (2) the residual stage has been elaboratively considered based on the evolution of the rock particle breakage. Then, the proposed interface model is integrated into the ABAQUS finite element (FE) code with no need of explicitly building the rock-pile interface profile. The accuracy of the proposed method is validated through comparisons between the simulation results and the field observed results.

2 ASSUMPTIONS FOR THE PROPOSED MODEL

2.1 Boundary conditions

Two common types of boundary conditions are typically used in direct shear tests, namely constant normal load (CNL) and constant normal stiffness (CNS). The CNL condition is suitable for studying planar and non-reinforced slope stability issues (Johnston and Lam 1989). However, for the analysis of rock-socketed piles under axial loading, the downward motion of the pile reduces the contact area at the interface while the pile undergoes dilation due to the confinement of the socket wall. As a result, normal stress is not constant but increases with the development of dilation, as depicted in Fig. 1. Hence, it is more appropriate to apply the CNS condition to model the shear behavior of the rock-pile interface. To incorporate this condition in the interface model, a spring is employed to represent the CNS boundary condition. The stiffness of the spring can be determined based on the expanding infinite cylinder theory in an elastic half-space, as outlined by Johnston and Lam (1989):

$$K = \frac{\Delta\sigma_n}{\Delta r} = \frac{E}{R(1+v)} \tag{1}$$

where K is the spring stiffness; E is the elastic modulus of the rock; R is the radius of the pile shaft, v is the Poisson's ratio.

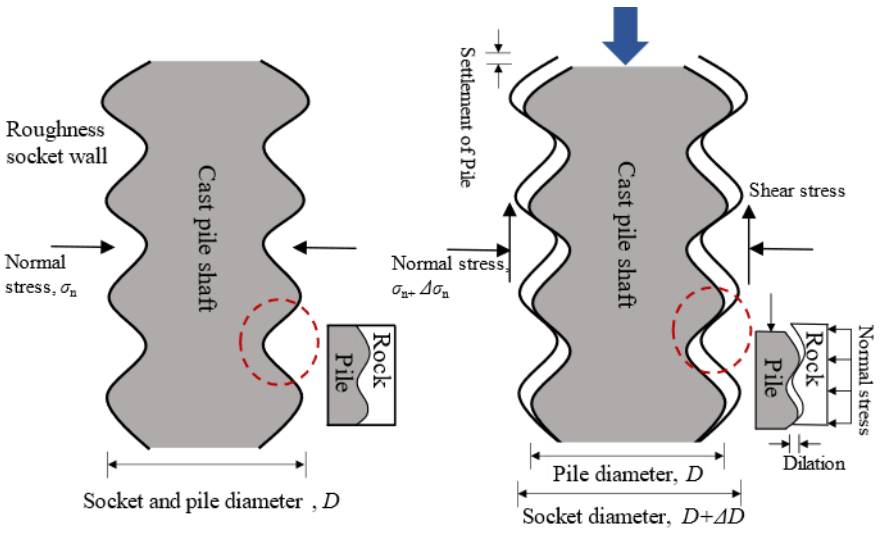

(a) (b)

Fig. 1. Bored pile socket into rocks: (a) initial rock-pile interface after casting; (b) pile settlement after axial loading

2.2 Idealized profile of the interface model

It is worth noting that the use of a uniform simplified surface can result in synchronized shear behavior of each asperity, encompassing both the pre-peak and post-peak stages. However, in natural rock boreholes, the shear behavior of individual asperities occurs separately, and each asperity contributes to the overall global shear stress independently (Zhao et al. 2021). To address this limitation, an idealized nonuniform triangular surface with the same inclined angle, θ, is proposed to represent the complex rock profiles, as illustrated in Fig. 2. For instance, considering a pile-rock interface with a nominal length of L, the length of a series of asperities can be determined through linear interpolation in an ascending sequence within the range of the minimum and maximum asperity lengths. The chord length of the i th ($1 \le i \le n$) asperity can be expressed as follows:

$$2\lambda_i = 2\lambda_1 + \frac{(2\lambda_n - 2\lambda_1)(i-1)}{n-1} \tag{2}$$

where n is the number of the asperities and $n=L/(\lambda_1+\lambda_n)$; $2\lambda_1$ and $2\lambda_n$ denote the minimum and maximum asperity length, respectively, which can be estimated by field-scanned borehole surface.

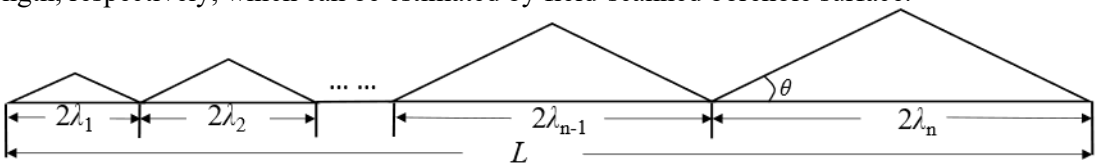

Fig. 2. Sketch of the uniform triangular rock-pile profile

2.3 Single asperity and multi-asperity behavior

The basic friction law can be employed to describe these two stages of shear behavior (Patton 1966):

$$\begin{cases} \tau = \sigma_n \tan(\varphi_i + \theta) \\ \tau_r = \sigma_n \tan(\varphi_r) \end{cases} \tag{3}$$

where τ and τ_r denote the shear stress in the dilation and post-peak stage; φ_i and φ_r are the base friction and residual friction angles; θ is the asperity inclination angle; σ_n represents the normal stress, which is related to the initial normal stress σ_{n0}, dilation displacement, y and spring stiffness, K. The relationship can be expressed as:

$$\sigma_n = \sigma_{n0} + Ky = \sigma_{n0} + Kw\tan\theta \tag{4}$$

where the dilatancy displacement, y, is equal to $w\tan\theta$; w is the relative shear displacement of the interface.

When combining a series of incremental-length asperities at the rock interface, the lift-off behavior needs to be considered. To be specific, as the dilation progresses, the initially closely contacted asperities would be separated, the smaller asperities will lose contact and undertake no more shear stress, as indicated in Fig. 3.

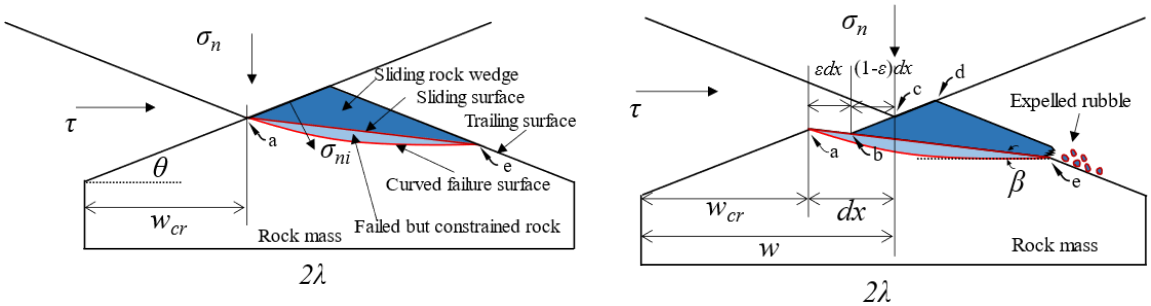

(a) single rock asperity at the critical state (b) newborn wedge slides along the failure surface

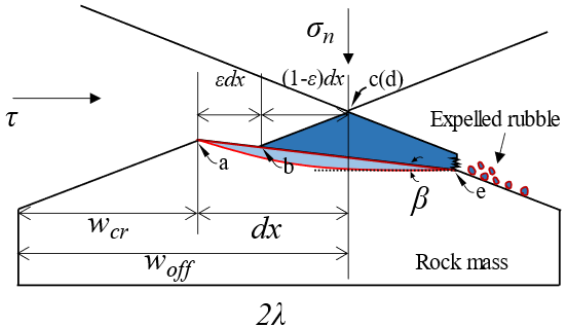

(c) local lift-off of the newly generated wedge

Fig. 3. Shear development of the newborn sliding wedge

3. DERIVATION OF THE MICROMECHANICS-BASED INTERFACE MODEL

3.1 Critical shear displacement with Hoek-Brown model

In this study, the rock mass is regarded as a Hoek-Brown material, the Hoek-Brown failure criterion is defined as follows (Hoek and Brown 2019):

$$\sigma_1' = \sigma_3' + \sigma_{ci}\left(m_b \frac{\sigma_3'}{\sigma_{ci}} + s\right)^a \tag{5}$$

where σ_1' and σ_3' are the major and minor effective principal stresses at failure, respectively; σ_{ci} is the unconfined compressive strength (UCS) of the intact rock mass; m_b is the reduced material parameter derived from m_i for intact rock mass; s and a are the parameters that rely upon the rock mass characteristics. These parameters are functions of the geological strength index (GSI) and can be calculated as follows:

$$\begin{cases} m_b = m_i \exp\left(\dfrac{GSI-100}{28-14D}\right) \\ s = \exp\left(\dfrac{GSI-100}{9-3D}\right) \\ a = \dfrac{1}{2} + \dfrac{1}{6}\left[\exp\left(\dfrac{-GSI}{15}\right) - \exp\left(\dfrac{-20}{3}\right)\right] \end{cases} \tag{6}$$

where D is the disturbance coefficient which varies from 0 for undistributed rock mass to 1 for highly disturbed rock mass; m_i is the constant of the intact rock which counts mainly on lithology and mineralogy of rock and can be obtained from experimental measurements. For intact rock, the constants can be set as s = 1 and a = 0.5.

The ultimate bearing capacity of the weightless rock asperity can be written as (Serrano and Olalla 1994):

$$p_c = \beta\left(N_\beta - \zeta\right) \tag{7}$$

where β and ζ are constants and $\beta = m_b\sigma_c/8$, $\zeta = 8s/m_b^2$; N_β is the parameter of bearing capacity and $N_\beta = \left(\cot^2\rho_A\right)/2 + \left(1-\sin\rho_A\right)/\sin\rho_A$; ρ_A is the instantaneous friction angle of zone A.

Following Serrano and Olalla (1994), the stress state associated with the α characteristic line (i.e., Riemann's invariant) can be expressed by Eq. (8) taking into account the Hoek-Brown failure criteria:

$$\frac{1}{2}\left[\cot\rho + \ln\left(\cot\left(\rho/2\right)\right)\right] + \psi = I \tag{8}$$

where ρ is the instantaneous friction angle, defined as ρ=arcsin(dq/dp), where p and q represent the mean stress and deviatoric stress in the plane, respectively; ψ denotes the counterclockwise rotation angle from x-

axis to major principal stress; I is the integration constant. Consequently, the stress state in both zone A and zone B can be interconnected by the following relationship:

$$\frac{1}{2}\left[\cot\rho_A+\ln\left(\cot\left(\rho_A/2\right)\right)\right]+\psi_A=\frac{1}{2}\left[\cot\rho_B+\ln\left(\cot\left(\rho_B/2\right)\right)\right]+\psi_B=I \tag{9}$$

where ρ_B is the instantaneous friction angle of zone B and can be calculated as $\rho_B=\sin^{-1}\left(1/\left(1+\sqrt{2\zeta}\right)\right)$. In this analysis, $\psi_B-\psi_A=\delta\text{-}\pi/2$. This equation is used to determine the value of ρ_A.

The normal stress on the asperity surface, σ_{ni}, gradually increases with the onward shearing, resulted the dislocation of the asperity and the occurrence of dilation under the CNS boundary condition. When σ_{ni} equals to the ultimate bearing capacity, p_c, the rock asperity enters the critical state. At this point, the asperity undergoes failure and is sheared off, as illustrated in Fig. 3(a) and (b). The value of σ_{ni} at failure can be determined as:

$$\sigma_{ni}=\frac{2\lambda\left(\sigma_n\cos\theta+\tau\sin\theta\right)}{\lambda-w_{cr}} \tag{10}$$

where w_{cr} is the critical shear displacement and can be derived considering $\sigma_{ni}=p_c$ by substituting Eq. (7) and Eq. (10):

$$w_{cr}=\frac{p_c\lambda-2\lambda\sigma_{n0}\left(\cos\theta+\tan\left(\varphi_i+\theta\right)\sin\theta\right)}{2\lambda K\tan\theta\left(\cos\theta+\tan\left(\varphi_i+\theta\right)\sin\theta\right)+p_c} \tag{11}$$

In the multi-asperity model, the shear-off criterion, $f\left(w_i^{cr},\lambda_i\right)$, can be given by:

$$f\left(w_i^{cr},\lambda_i\right)=w-w_i^{cr}=w-\frac{p_c\lambda-2\lambda\sigma_{n0}\left(\cos\theta+\tan\left(\varphi_i+\theta\right)\sin\theta\right)}{2\lambda K\tan\theta\left(\cos\theta+\tan\left(\varphi_i+\theta\right)\sin\theta\right)+p_c} \tag{12}$$

where the subscript i is the asperity index, when $f\left(w_i^{cr},\lambda_i\right)=0$ indicates the failure of i-th asperity.

No sooner had the largest asperity been sheared off than the normal displacement changing from dilation to contraction. A noteworthy aspect of this study is the behavior of the granular material, which is detached from the rock. As depicted in Fig. 4, the separated granular material experiences compression and exhibits translation and rotation at the interfaces with the concrete and rock boundaries.

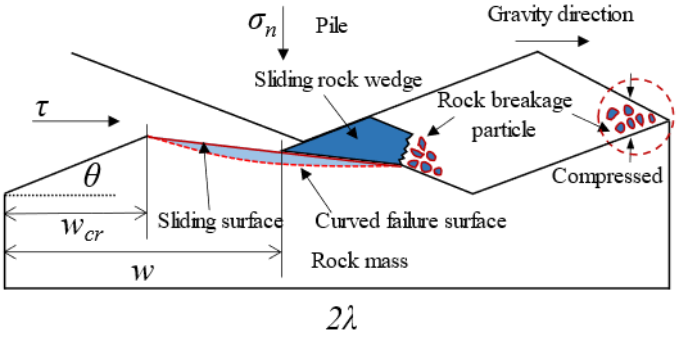

Fig. 4. Local compression after the largest asperity has been sheared off

In order to provide a detailed illustration of this influence on shearing behavior, the red dashed line circle area in Fig. 4 is magnified and shown in Fig. 5. For simplicity, a single rock particle is selected as a representative to analyze the transformation of its morphology. Based on observations from rock compression and sliding tests (Seidel and Haberfield 2002, Gehle and Kutter 2003, Zhu et al. 2010, Xu et al. 2020, Zhao et al. 2023), the hypothetical evolution of particle shape with compression and sliding is depicted in Fig. 5 (a)–(c). The granular material will gradually experience rounding with an increasing shearing displacement, resulting in a lower shear resistance on account of the transition from sliding friction to rolling friction in the global frictional behavior.

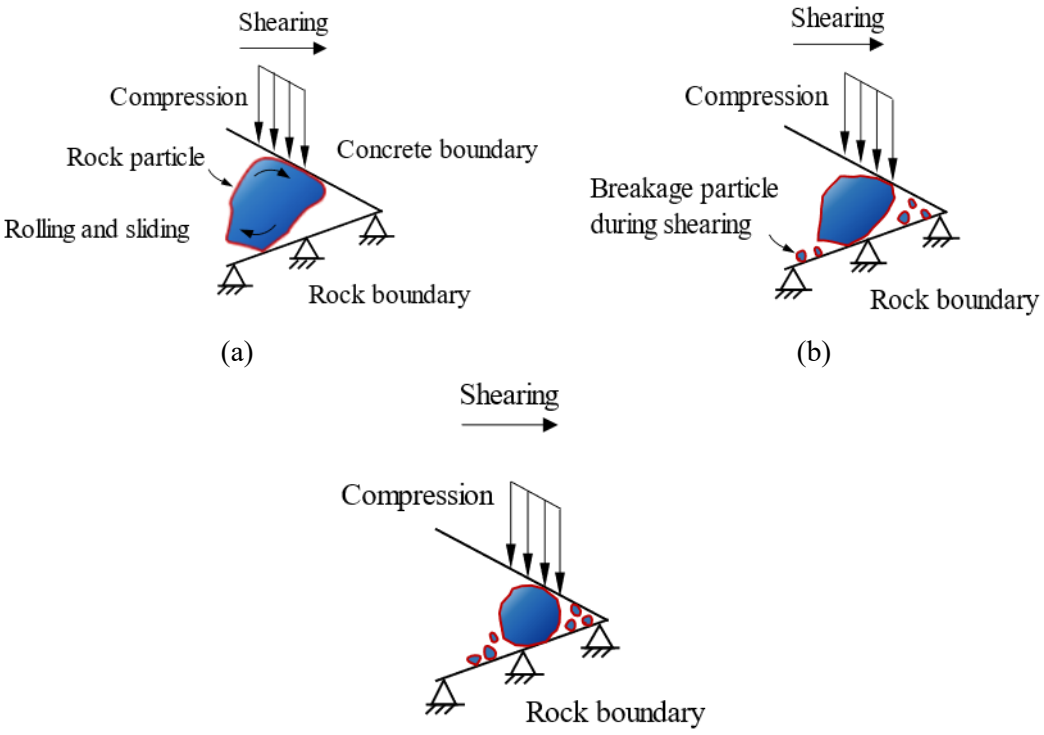

Fig. 5. Evolution of particle shape with shearing

However, there is currently no established method for quantifying this friction mechanism. Therefore, a novel friction parameter, μ^*, is proposed to describe the shear behavior after the largest asperity has been sheared off, as shown below:

$$\begin{cases} \mu^* = \left(1 - B_r^*\right)\kappa + B_r^* \mu_r \\ B_r^* = \dfrac{w - w_{\max}^{cr}}{b + w - w_{\max}^{cr}} \end{cases} \tag{13}$$

where κ is the friction coefficient after the single asperity has been sheared off; μ_r is the residual friction parameter, $\mu_r = \tan\varphi_r$, φ_r is the residual interface friction angle; B_r^* is the friction degradation factor, which is related to the shear displacement, w, the critical displacement of the largest asperity, $w_{\max}^{cr}$ and a constant, b, which controls the rate of degradation.

3.2 Schematic representation of calculation result of proposed model

The schematic representation of the calculation results showing the relationship between shear displacement and shear stress using this interface model is presented in Fig. 6. The plot shows the progression of shear in three stages, separated by the two critical displacements. To be specific, in stage 1, the shear stress shows a linear increase with shearing until the minimum asperity is sheared off. In stage 2, as the asperities progressively shear off, there shows an abrupt change in local stress, leading to stress oscillation. After reaching the peak shear stress, a degradation trend is observed on account of the dominance of lift off in the shear behavior. The system enters stage 3 once the shear displacement meets the maximum critical shear displacement, indicating that all the asperities have been sheared off. In stage 3, the shear stress gradually decreases until it stabilizes.

Proceedings DOI: 10.21467/proceedings.7.7

Series: AIJR Proceedings
ISBN: 978-81-989164-3-3
ISSN: 2582-3922

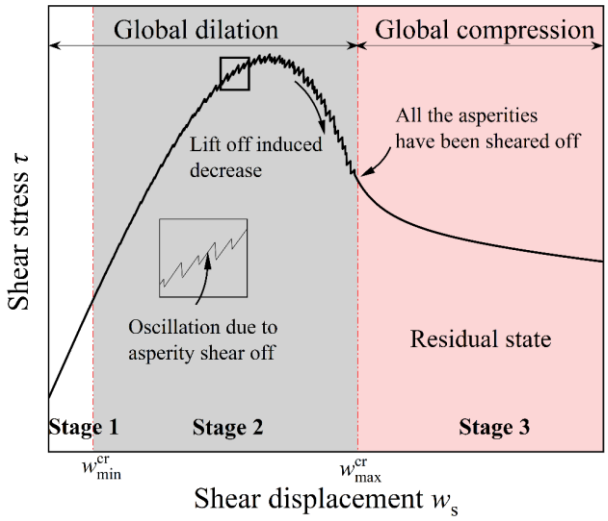

Fig. 6. Schematic representation of calculation result of proposed model

4 FINITE ELEMENT IMPLEMENTATION

4.1 Finite element model of the rock-socketed pile

Fig. 7 shows the schematic and mesh details of the typical axial loaded rock-socketed pile model, incorporating the user-defined interface model. For simplicity, this model is interpreted as 2D axisymmetric. The model has with a width of 20 times the pile diameter, D, and a height of 2 times the socket length, L, from the socket head to the bottom boundary. The model scale is chosen to be large enough to ignore the boundary effects on pile axial bearing performance (Liang et al. 2021). The tangential behavior between the pile shaft and socket wall is simulated using the user-defined interface model proposed in this study. The pile is assigned an isotropic linear elastic material. The socket and bearing layer are assigned the Hoek-Brown material via using the user material subroutine UMAT following Clausen and Damkilde (2008). The vertical boundary on the left side is an asymmetrical line, while the roller boundary and the fixed boundary are applied on the side and bottom of the model, respectively. A denser mesh is employed near the pile and a coarser mesh is adopted far away from the pile to minimize the influence of the stress concentration and enhance the calculation efficiency. The analysis utilizes four-node bilinear axis-symmetric finite elements (CAX4). In the model verification process, the geostatic step is calculated to establish the initial stress state. After the equilibrium of the geostatic, the equivalent axial pressure is applied with displacement controlled axial loading on the socket head.

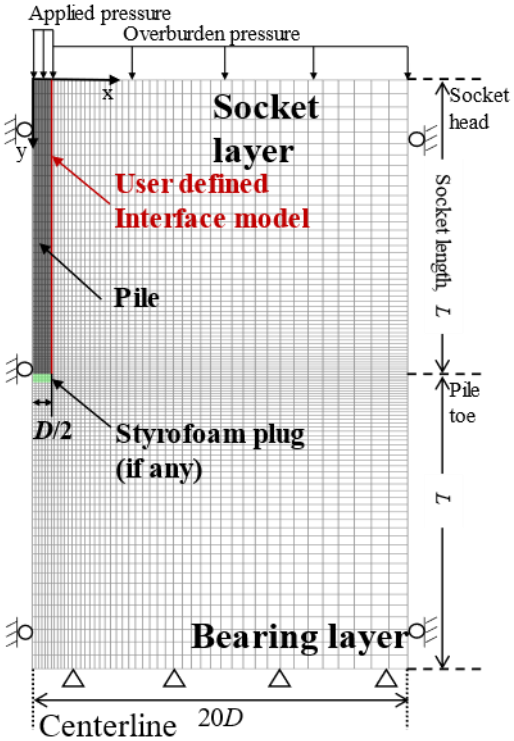

Fig. 7. Schematic representation for the typical 2D axisymmetric axial loaded rock-socketed pile FE model

The flow chart that outlines the user-defined subroutine FRIC for the interface model developed in this study is plotted in Fig. 8. The subroutine takes the constants of the proposed model and the variables computed from ABAQUS as inputs. The subroutine examines the contact pressure (PRESS) and the relative motion flag (LM) to determine the contact status of interface elements and if relative motion is permitted (if the contact point can slip, LM is assigned a value of 0; if the contact point is sticking, LM is equal to 1; if the contact is open, LM is equal to 2). If the conditions are satisfied, the subroutine calculates the shear stress (TAU(1)) and shear stiffness (DDTDDG(1,1)), which are subsequently updated in the main program.

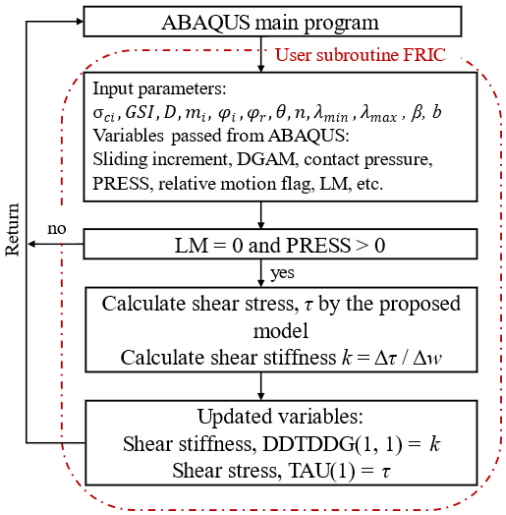

Fig. 8. The flowchart of the user-defined subroutine framework of the proposed analysis

4.2 Application to field cases

4.2.1 Case 1

The shaft under investigation was situated in downtown Dallas, Texas, and the field test was conducted

by O'Neill et al. (1996) The sub-soils of the site consisted primarily of a 3 m thick layer of fill, followed by the undisturbed clay-shale with calcareous pockets. The socket was excavated by the soil auger, and the diameter of the tested pile was 0.61 m. The pile was embedded to a depth of 9.44 m, with a socket length of 6.44 m. A Styrofoam plug measuring 0.15 m in thickness was placed beneath the pile toe to exclude base resistance and ensure the complete mobilization of the shaft resistance. Fig. 9(a) provides an illustrative idealized depiction of the cast-in-place pile. The model parameters and interface properties are summarized in Table. 2.

4.2.2 Case 2

The static load test was conducted on bored pile socket into the conglomerate by Skejić et al. (2022) The geotechnical site characterization revealed a layer of sandy gravel and cobbles with a thickness of 4 meters, succeeded by a 7-meter-thick layer of poorly cemented conglomerate, and a transition to well-cemented conglomerate. The combined drilling method, core barrel and casting were utilized to create the borehole. An instrumented pile with a diameter of 0.9 m and an embedded length of 10 m was then constructed. To eliminate any contribution from shaft resistance above the socket level, a steel sleeve with a length of 7 m was installed. Additionally, a 10 cm thick layer of Styrofoam was placed under the pile toe prior to installation, as shown in Fig. 9(b).

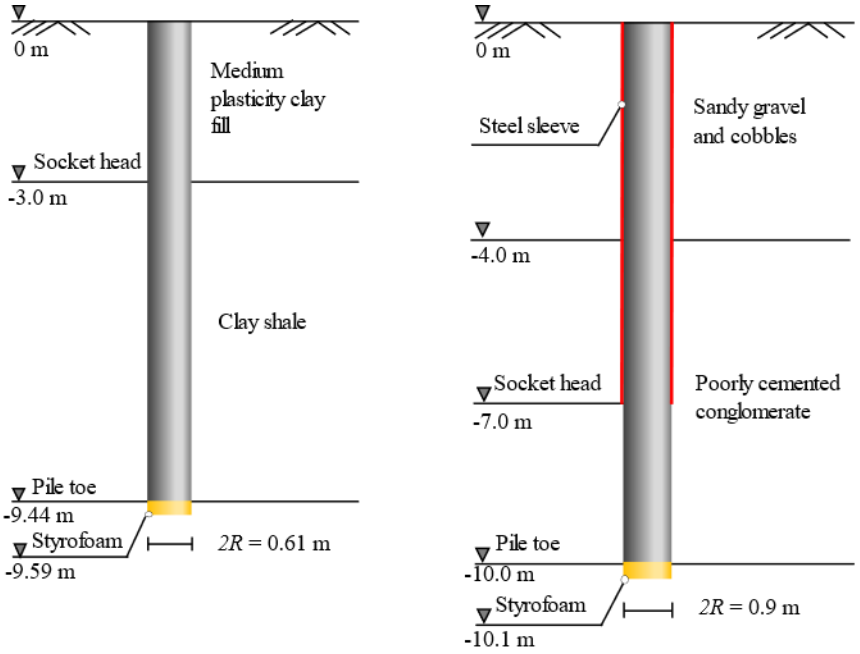

(a) (b)

Fig. 9. Sketch of cast-in-place test pile for different cases: (a) Case 1; (b) Case 2

4.3 Parameters for analysis and comparison results

The material parameters and the interface parameters that are chosen for the finite element analysis based on the field test are summarized in Table 1. The parameters for Hoek-Brown failure criteria, including s_{ci}, GSI, m_i and D are determined following the methods proposed by Hoek and Brown (Hoek and Brown 1997, 2019) and Hoek et al. (2002) The interface profile parameters, such as q , n, l_{min}, and l_{max}, are determined from field-measured borehole roughness. Horvath et al. (1980) defined the roughness factor (RF) to quantify the roughness of the rock socket interface, as shown in Eq. (14).

$$RF = \frac{h_m L_t}{R_s L} \tag{14}$$

where R_s is the radius of the socket; h_m, L_t and L represent the average asperity height, travel length and nominal length along the socket side wall, respectively. These parameters can be determined from field

scanned roughness data. The calculated *RF* for this idealized nonuniform interface profile can be used to provide additional verification by comparing it to the field-measured *RF*.

Importantly, the laser-based profiling scanning technique estimated the quantitative socket roughness (*RF*) to be 0.0215 in Case 2 (Skejić et al. 2022). Remarkably, the calculated *RF* using the proposed interface model closely matches the site-measured value, with a value of 0.0216. This congruence between the calculated and measured *RF* values provides strong validation for the effectiveness of the proposed profile. Similarly, the calculated *RF* for Case 1 is 0.0076, consistent with the essentially smooth field-measured profile (O'Neill et al. 1996).

Table 1 Material and interface parameters used for finite element analysis

Case	Material type	E MPa	v	σ_{ci} [(b)] MPa	GSI [(b)]	m_i [(b)]	D [(b)]	φ_i °	φ_r °	θ [(c)] °	n [(c)]	λ_{min} [(c)] mm	λ_{max} [(c)] mm	β [(d)] °	b	RF
Case 1																
Socket	Hoek-Brown	232	0.3	1	30	5	0	-	-	-	-	-	-	-	-	-
Pile	Linear elastic	27600	0.3	-	-	-	-	-	-	-	-	-	-	-	-	-
Styrofoam	Linear elastic	10[(a)]	0.3 [(e)]	-	-	-	-	-	-	-	-	-	-	-	-	-
Interface	User-defined	232	0.3	1	30	5	0	30	24	10	100	1	10	-2.4	0.5	0.0076
Case 2																
Socket	Hoek-Brown	1500	0.25	9	50	22	0	-	-	-	-	-	-	-	-	-
Pile	Linear elastic	15000	0.3	-	-	-	-	-	-	-	-	-	-	-	-	-
Styrofoam	Linear elastic	10[(a)]	0.3 [(e)]	-	-	-	-	-	-	-	-	-	-	-	-	-
Interface	User-defined	1500	0.25	9	50	22	0	58	56	30	100	2	25	-5	0.5	0.0216

[(a)] Predicted value by E=0.0097ρ^2–0.014ρ+1.8, ρ is the Styrofoam density (Eriksson and Trank 1991)

[(b)] When field or laboratory tests are unavailable, σ_{ci}, GSI, m_i and D can be estimated from Hoek and Brown (Hoek and Brown 1997, 2019, Hoek et al. 2002)

[(c)] Determined from field measured roughness and verified with roughness factor (RF) (Horvath et al. 1980)

[(d)] Estimated from Seidel and Haberfield (2002)

[(e)] Estimated from Dai et al. (2017)

Fig. 10 presents the measured and simulated axial load distributions with socket depth for the two cases. The FE analysis results predicted by proposed model demonstrates good agreement with the field measurement, capturing the overall load transfer trend accurately. It is clearly observed that as the axial load increases, a substantial portion of the shaft friction is contributed by the upper section of the socket, gradually diminishing towards the pile toe.

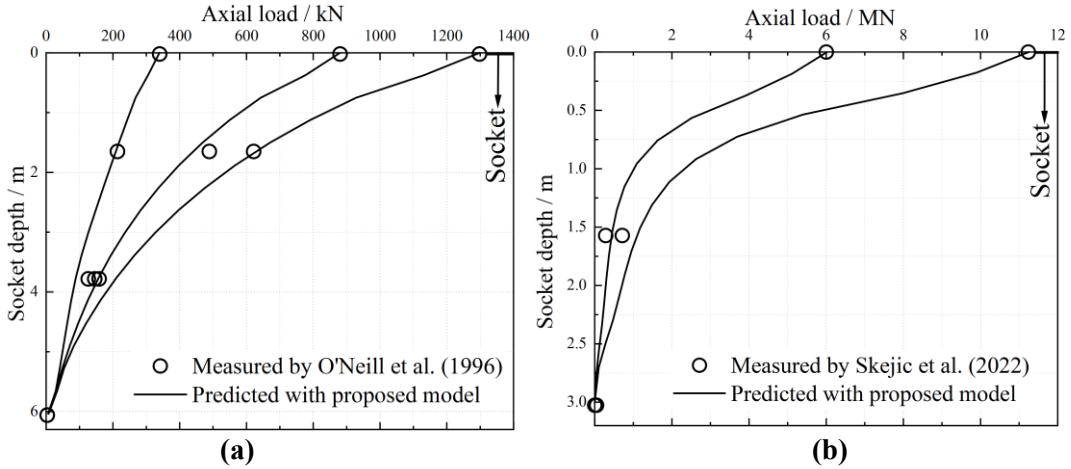

Fig. 10. Simulated and measured axial load distributions with socket depth (a) Case 1; (b) Case 2

5 CONCLUSIONS

This paper provided an enhanced method to estimate the load transfer behavior for the drilled shaft embedded in weak rocks. The micromechanics-based interface model with nonuniform profile was

thoughtfully developed with two enhancements. Slip line method combined with nonlinear failure criteria was integrated to derive the critical shear displacement for single rock asperity. The residual state of shearing was well considered based on the evolution of the sheared off debris with the novel friction parameter being proposed. The general shear constitutive function was divided into two scenarios, i.e., global dilation and global compression, to calculate the shear stress. This interface model can be implemented as a user-defined subroutine into the finite element code ABAQUS. This implementation does not require external elaboration to explicitly build the rock-pile interface profile. The applicability of this method was well examined with field-monitored results from literature, in which the axial bearing capacity of the pile was effectively captured.

ACKNOWLEDGEMENTS

The work presented in this paper is supported by the Research Grants Council (RGC) of Hong Kong Special Administrative Region Government (HKSARG) of China (RIF: R5037-18; GRF: 15210020, 15221721, and 15226722).

REFERENCES

Akgüner, C., and Kirkit, M. 2012. Axial bearing capacity of socketed single cast-in-place piles. Soils and Foundations, **52**(1): 59–68. doi:10.1016/j.sandf.2012.01.012.

BD (Buildings Department Technical Committee of Hong Kong). 2017. Code of practice for foundations 2017 of Hong Kong.

Carrubba, P. 1997. Skin friction on large-diameter piles socketed into rock. Canadian Geotechnical Journal, **34**(2): 230–240. doi:10.1139/t96-104.

Carter, J.P., and Kulhawy, F.H. 1988. Analysis and design of drilled shaft foundations socketed into rock.

Castelli, F., Maugeri, M., and Motta, E. 1992. Analisi non lineare del cedimento di un Palo Singolo. RIG, **2**: 92.

Chen, Z.-J., Chen, W.-B., Yin, J.-H., and Malik, N. 2021. Shaft Friction Characteristics of Two FRP Seawater Sea–Sand Concrete Piles in a Rock Socket with or without Debris. International Journal of Geomechanics, **21**(7): 06021015. doi:10.1061/(ASCE)GM.1943-5622.0002059.

Clausen, J., and Damkilde, L. 2008. An exact implementation of the Hoek–Brown criterion for elasto-plastic finite element calculations. International Journal of Rock Mechanics and Mining Sciences, **45**(6): 831–847. doi:10.1016/j.ijrmms.2007.10.004.

Dai, G., Salgado, R., Gong, W., and Zhu, M. 2017. The effect of sidewall roughness on the shaft resistance of rock-socketed piles. Acta Geotechnica, **12**(2): 429–440. doi:10.1007/s11440-016-0470-8.

Dykeman, P., and Valsangkar, A.J. 1996. Model studies of socketed caissons in soft rock. Canadian Geotechnical Journal, **33**(5): 747–759. doi:10.1139/t96-100-321.

Eriksson, L., and Trank, R. 1991. Properties of expanded polystyrene, laboratory experiments. Swedish Geotechnical Institute, Linköping, Sweden,.

Gehle, C., and Kutter, H.K. 2003. Breakage and shear behaviour of intermittent rock joints. International Journal of Rock Mechanics and Mining Sciences, **40**(5): 687–700. doi:doi.org/10.1016/S1365-1609(03)00060-1.

Hoek, E., and Brown, E.T. 1997. Practical estimates of rock mass strength. International Journal of Rock Mechanics and Mining Sciences, **34**(8): 1165–1186. doi:10.1016/S1365-1609(97)80069-X.

Hoek, E., and Brown, E.T. 2019. The Hoek–Brown failure criterion and GSI–2018 edition. Journal of Rock Mechanics and Geotechnical Engineering, **11**(3): 445–463. doi:10.1016/j.jrmge.2018.08.001.

Hoek, E., Carranza-Torres, C., and Corkum, B. 2002. Hoek-Brown failure criterion-2002 edition. Proceedings of 5th North American Rock Mechanics Symposium,: 267–273.

Horvath, R.G., Kenney, T.C., and Trow, W.A. 1980. Results of tests to determine shaft resistance of rock-socketed drilled piers. *In* International Conference on Structural Foundations on Rock.

Johnston, I.W., and Lam, T.S. 1989. Shear behavior of regular triangular concrete/rock joints—analysis. Journal of Geotechnical Engineering, **115**(5): 711–727. doi:10.1061/(ASCE)0733-9410(1989)115:5(711).

Kou, H.-L., Guo, W., Zhang, M.-Y., and Xu, Y.-Q. 2016. Axial resistance of long rock-socketed bored piles in stratified soils. Ocean Engineering, **114**: 58–65. doi:10.1016/j.oceaneng.2016.01.013.

Leung, C.F., and Ko, H.Y. 1993. Centrifuge model study of piles socketed in soft rock. Soils and Foundations, **33**(3): 80–91. doi:10.3208/sandf1972.33.3_80.

Li, Y.-C., Sun, S.-Y., and Tang, C.-A. 2019. Analytical prediction of the shear behaviour of rock joints with quantified waviness and unevenness through wavelet analysis. Rock Mechanics and Rock Engineering, **52**(10): 3645–3657. doi:10.1007/s00603-019-01817-5.

Liang, R., Yuan, Y., Fu, D.-F., and Liu, R. 2021. Cyclic response of monopile-supported offshore wind turbines under wind and wave loading in sand. Marine Georesources & Geotechnology, **39**(10): 1230–1243. doi:10.1080/1064119X.2020.1821848.

Ng, C.W., Yau, T.L., Li, J.H., and Tang, W.H. 2001. Side resistance of large diameter bored piles socketed into decomposed rocks. Journal of Geotechnical and Geoenvironmental Engineering, **127**(8): 642–657. doi:10.1061/(ASCE)1090-0241(2001)127:8(642).

Omer, J.R., Delpak, R., and Robinson, R.B. 2002. Instrumented load tests in mudstone: pile capacity and settlement prediction. Canadian Geotechnical Journal, **39**(6): 1254–1272. doi:10.1139/t02-072.

O'Neill, M.W., and Hassan, K.M. 1994. Drilled shafts: Effects of construction on performance and design criteria. *In* Proc., Int. Conf. Des. Constr. Deep Founds. Orlando, FHWA.

O'Neill, M.W., Townsend, F.C., Hassan, K.M., Buller, A., and Chan, P.S. 1996. Load transfer for drilled shafts in intermediate geomaterials.

Patton, F.D. 1966. Multiple modes of shear failure in rock. *In* 1st ISRM Congress.

Seidel, J.P., and Haberfield, C.M. 2002. A theoretical model for rock joints subjected to constant normal stiffness direct shear. International Journal of Rock Mechanics and Mining Sciences, **39**(5): 539–553. doi:10.1016/S1365-1609(02)00056-4.

Seol, H., Jeong, S., and Cho, S. 2009. Analytical method for load-transfer characteristics of rock-socketed drilled shafts. Journal of Geotechnical and Geoenvironmental Engineering, **135**(6): 778–789. doi:10.1061/(ASCE)1090-0241(2009)135:6(778).

Serrano, A., and Olalla, C. 1994. Ultimate bearing capacity of rock masses. *In* International Journal of Rock Mechanics and Mining Sciences & Geomechanics Abstracts.

Skejić, A., Gavrić, D., Jurišić, M., and Rahimić, Đ. 2022. Experimental and Numerical Analysis of Axially Loaded Bored Piles Socketed in a Conglomerate Rock Mass. Rock Mechanics and Rock Engineering, **55**(10): 6339–6365. doi:10.1007/s00603-022-02932-6.

Tian, H.M., Chen, W.Z., Yang, D.S., and Yang, J.P. 2015. Experimental and numerical analysis of the shear behaviour of cemented concrete–rock joints. Rock Mechanics and Rock Engineering, **48**(1): 213–222. doi:10.1007/s00603-014-0560-6.

Williams, A.F. 1980. The design and performance of piles socketed into weak rock.

Xu, J., Haque, A., Gong, W.M., Gamage, R.P., Dai, G., Zhang, Q., and Xu, F. 2020. Experimental study on the bearing mechanisms of rock-socketed piles in soft rock based on micro X-ray CT analysis. Rock Mechanics and Rock Engineering, **53**(8): 3395–3416. doi:10.1007/s00603-020-02121-3.

Zhan, C.-Z., and Yin, J.-H. 2000. Field static load tests on drilled shaft founded on or socketed into rock. Canadian Geotechnical Journal, **37**(6): 1283–1294. doi:10.1139/t00-048.

Zhao, H., Hou, J.-C., Zhang, L., and Zhao, M. 2021. Towards concrete-rock interface shear containing similar triangular asperities. International Journal of Rock Mechanics and Mining Sciences, **137**: 104547. doi:10.1016/j.ijrmms.2020.104547.

Zhao, H., Hou, J.C., and Zhao, M.-H. 2022. A micromechanics-based model for concrete-rock interface with similar triangular asperities. International Journal of Rock Mechanics and Mining Sciences, **157**: 105183. doi:10.1016/j.ijrmms.2022.105183.

Zhao, L.-Y., Lv, Z.-M., Lai, Y.-M., Zhu, Q.-Z., and Shao, J.-F. 2023. A new micromechanical damage model for quasi-brittle geomaterials with non-associated and state-dependent friction law. International Journal of Plasticity, **165**: 103606. doi:10.1016/j.ijplas.2023.103606.

Zhu, Q.Z., Shao, J.F., and Mainguy, M. 2010. A micromechanics-based elastoplastic damage model for granular materials at low confining pressure. International Journal of Plasticity, **26**(4): 586–602. doi:10.1016/j.ijplas.2009.09.006.

ISBN: 978-81-989164-3-3 ISSN: 2582-3922